Automatic Satellite Image Georeferencing Using a Contour-Matching Approach

Francisco Eugenio, *Associate Member, IEEE*, and Ferran Marqués, *Member, IEEE*

***Abstract*—Multitemporal and multisatellite studies or comparisons between satellite data and local ground measurements require nowadays precise and automatic geometric correction of satellite images. This paper presents a fully automatic geometric correction system capable of georeferencing satellite images with high accuracy. An orbital prediction model, which provides initial earth locations, is combined with the proposed automatic contour-matching technique. This combination allows correcting the low-frequency error component, mainly due to timing and orbital model errors, as well as the high-frequency error component, due to variations in the spacecraft's attitude. The approach aims at exploiting the maximum reliable information in the image to guide the matching algorithm. The contour-matching process has three main steps: 1) estimation of the gradient energy map (edges) and detection of the cloudless (reliable) areas; 2) initialization of the contours positions; 3) estimation of the transformation parameters (affine model) using a contour optimization approach. Three different robust and automatic algorithms are proposed for optimization, and their main features are discussed. Finally, the performance of the three proposed algorithms is assessed using a new error estimation technique applied to Advanced Very High Resolution Radiometer (AVHRR), Sea-viewing Wide Field of view Sensor (SeaWiFS), and multisensor AVHRR–SeaWiFS imagery.**

***Index Terms*—Advanced Very High Resolution Radiometer (AVHRR), contour optimization, feature extraction, image georeferencing, multitemporal and multisensor images, remote sensing image processing, Sea-viewing Wide Field of view Sensor (SeaWiFS).**

I. Introduction

CURRENTLY, there is a continuing need for accurate, efficient, and autonomous geometric correction algorithms [1]. Some of the reasons are the increasing complexity of contemporary remote sensing systems (some of which have significantly off-nadir viewing capabilities, e.g., National Oceanic and Atmospheric Administration (NOAA) Advanced Very High Resolution Radiometer (AVHRR) and SeaStar Sea-viewing Wide Field of view Sensor (SeaWiFS), the interest in multitemporal and multisatellite studies, and the increasing requirements of earth scientists for precision, temporal resolution and repeatability of remote sensing measurements.

Manuscript received September 28, 2002; revised May 3, 2003. This work was supported by the CICYT-Commission of the European Communities under Project 1FD97–1167 and by the National Aeronautics and Space Administration under the SeaWiFS Project.

F. Eugenio is with the Signal and Communications Department, University of Las Palmas of Gran Canaria, Campus Universitario de Tafira, Edificio de Telecomunicación, 35017 Las Palmas of Gran Canaria, Spain (e-mail: feugenio@dsc.ulpgc.es).

F. Marqués is with the Signal Theory and Communications Department, Technical University of Catalunya, 08034 Barcelona, Spain (e-mail: ferran@gps.tsc.upc.es).

Digital Object Identifier 10.1109/TGRS.2003.817226

In many image processing applications using satellite images and specifically in those related to oceanographic studies, it is necessary to compare multiple images of the same scene acquired by different sensors or images taken by the same sensor but at different time instants [2], [3]. Typical applications include multitemporal classification, recognition, and tracking of specific patterns, multisensor data fusion, and environment monitoring.

Such a comparison of multiple images requires either their spatial registration or their georeferencing. Several techniques for the registration (spatial alignment) of images from the same area have been proposed [4]–[11]. However, in the framework of oceanographic studies, the comparison of multitemporal and multisensor images is performed by the georeferencing of each image into a same geographic projection. Image georeferencing is the double process of correcting the remotely sensed image and transforming it into a known geographic projection (map coordinates) allowing the comparison with local ground measurements. This way, multisensor data georeferencing enables comparison and fusion of information from different sensory modalities, which often provide complementary information about the region surveyed.

The sea surface temperature (SST) and ocean color imagery remotely sensed by the AVHRR aboard the NOAA satellite series and by SeaWiFS aboard the SeaStar satellite are conveniently used in various fields, such as oceanography, meteorology, or fishery [12], [13]. AVHRR and SeaWiFS images are subjected to different geometric distortions due to the earth's curvature and rotation, the spacecraft's speed, altitude and attitude, and the scan skew. These distortions, if not properly accounted for, will prevent meaningful comparison among images.

For a good overview of existing methods for geometric correction of satellite imagery, the reader is referred to [1], [12], and [14]–[17]. In these works, several models of varying complexity, based on the satellites trajectories, can be found ranging from the locally circular orbit approach to complex elliptical orbits in which perturbations caused by the earth's oblateness, the gravitation effects of the sun and moon, etc., are taken into account. The accuracy obtained from the application of these models is variable. Failures in the satellite's internal clock, inaccuracies in Kepplerian orbital elements and lack of knowledge concerning the attitude angles, lead to that even the most complex models do not offer the desired accuracy of errors of less than one pixel. To achieve this precision, an additional step is commonly applied, using ground control points (GCPs), e.g., unique geographical locations or features such as small islands,

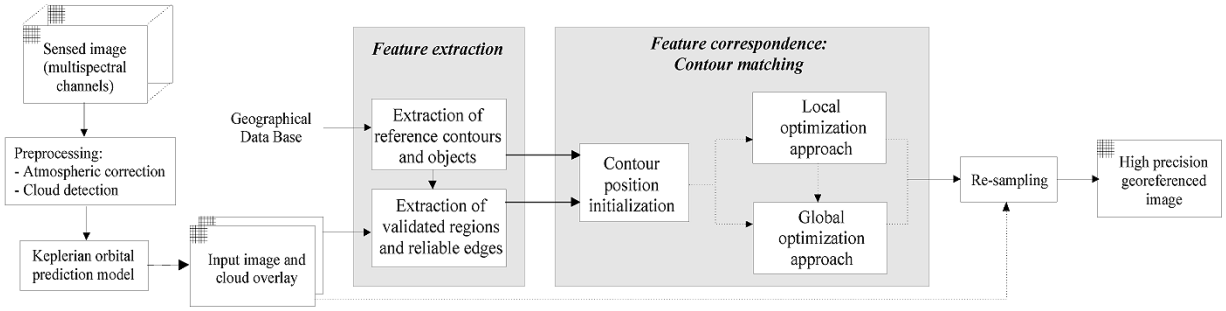

Fig. 1. Schematic procedure of the proposed automatic contour-matching system.

lakes, capes, etc., for each of which the location in the image can be identified and the location on a map is known [18]–[20].

GCP manual selection is extensively used in practical applications [21]–[23]. However, obtaining a reliable number of GCPs is a very tedious and labor-intensive work. Moreover, it is subject to inconsistency problems, limited accuracy, and, in many instances, lack of availability of GCPs due to partial or total occlusions. Thus, there is a critical need to develop automated techniques requiring little or no operator intervention to georeferencing multitemporal and/or multisensor images when higher accuracy is desired. Toward this goal, automatization by area-based techniques has been used in NOAA AVHRR image navigation [24], [25]. In these methods, a small window of points in the reference image is statistically compared with windows of the same site in the sensed image. The measure of similarity is usually the normalized cross correlation. However, correlation measures become unreliable when images have multiple partial or total occlusions and their gray-level characteristics vary, e.g., daytime and nighttime AVHRR data or SeaWiFS data [26].

In contrast, feature-based methods, typically used in image registration, are more robust and suitable in such cases. These techniques extract and match the common structures from two images, using region boundaries and other strong edges as matching primitives [6], [8].

This paper proposes two new feature-based approaches to automatic georeferencing remotely sensed images, as shown in Fig. 1, and explores their critical elements. These elements include (see Fig. 1) feature extraction, contour position initialization and feature correspondence by optimization of the reference image contours on the input image. To help understanding the proposed techniques, let us define two sets of terms that will be used throughout this paper.

- An *input image* is a sensed image (obtained by the satellite sensor), atmospherically corrected, which has been coarsely georeferenced only using an orbital prediction model. *Edges* are the estimated boundaries of an input image whereas *regions* are its homogeneous areas, which are obtained using a segmentation process.
- A *reference image* is a map in a specific projection containing the sea–land boundaries present in a geographical area, i.e., an overlay of geographic features such as coastlines. These sea–land boundaries will be referred to as *reference contours* and the areas defining these contours as *objects*, since they have a semantic meaning (islands, continent, ocean areas, etc.).

The proposed technique uses as main features all reliable edges (coastlines not occluded by clouds). This way, it matches all reliable edges with their corresponding reference contours. Prior to the feature correspondence process, the contour initialization step associates regions in the input image to their respective objects in the reference image and performs a uniform translation of the reference contours on the input image.

In the feature correspondence process, we present two contour-matching algorithms. The main difference between them is in the optimization scheme: the first scheme initially performs a set of local optimizations prior to obtaining the global parameters, whereas the second scheme carries out a multidimensional optimization that directly yields such global parameters. In a third scheme, both algorithms are combined to achieve subpixel accuracy. Finally, the input image is resampled using the global parameters. In this paper, the cases of AVHRR and SeaWiFS have been analyzed, but the proposed method is extendable to any sensor, e.g., the Terra Moderate Resolution Imaging Spectrometer (MODIS) and European Remote Sensing (ERS) Along Track Scanning Radiometer (ATSR), among others.

A common procedure to assess the quality of georeferencing techniques is to determine the RMS error in the georeferenced image of the set of GCPs used to obtain the transformation coefficients, as well as of an independent set of test control points [1], [18]. To overcome the problems above commented of this procedure, a new method has been developed based on the use of all the available image information, allowing us to achieve a more robust quantitative estimation of the accuracy of georeferenced images.

Finally, it has to be pointed out that both the proposed contour-matching technique and the georeferencing error estimation assume that a reference image containing the coastlines of the input image geographical area is available. This is a very common situation, and several geographical databases can be used to create such a reference image [27].[1].

This paper is organized as follows. Section II discusses the feature extraction procedure. Section III focuses on the contour-matching algorithms, describing the local optimization and the multidimensional global optimization schemes as well as the combined approach. Section IV details the error estimation technique proposed for assessing georeferencing results.

[1]See also http://www.ngdc.noaa.gov/mgg/gebco/gebco.html.

Fig. 2. Example of a reference image (coastlines) extracted from a geographic database (27° to 33° N, 8° to 19° W).

In Section V, some experimental results are presented and analyzed. The final conclusions are included in Section VI.

II. Feature Extraction

The proposed technique performs a contour initialization step that matches the objects in the reference image with their related regions in the input image. Afterward, the contour-matching approach aligns the reference contours with the reliable edges from the input image. Therefore, there are four different features that must be obtained: contours and objects from the geographical database and validated regions (identified land areas) and reliable edges (estimated sea–land boundaries) from the input image.

A. Extraction of Reference Contours and Objects

The reference image defining the reference contours of the area under analysis is created processing a geographical database. In our case, the overlay (reference image) is obtained from the geographical data available at the Central Intelligence Agency World Data Base II.[2] This database contains the geographical coordinates of precise geographical features such as coastlines and rivers. Coastline geographical coordinates are transformed to the desired projection (e.g., Mercator) following the classical approaches and, in our context, setting the spatial resolution of the transformation to 1.1 km, which corresponds to the AVHRR and SeaWiFS subsatellite resolution. With this information, a reference image containing the coastline position is created. In the process, reference contours are ensured to be closed, one-pixel width, eight connected contours.

Objects are easily obtained from the reference image given that contours are closed (taking into account the frame of the image defining the area under study). An example of reference image is illustrated in Fig. 2 where the reference contours are in black and the various objects in gray.

B. Extraction of Validated Regions and Reliable Edges

The presence of clouds (clutter) is a major problem in contour matching for accurate georeferencing, since it leads to matching errors and false detection. It is highly desirable to remove these irrelevant features before detection and analysis. In this work, the cloud overlay $[M(x,y)]$ is computed using the multiband threshold method proposed in [28], which has been extended and adapted to the region of analysis [25]. Other techniques could be used, since, as can be seen in Fig. 1, this is a preprocessing step that is not included in the feature extraction process.

Extraction of Validated Regions: Once the cloud areas have been extracted, land areas have to be detected. There is no unique segmentation technique that can perform best in all types of images, and most segmentation techniques are image dependent [4], [29]. For this application, we use an iterative threshold selection technique [29]. It is based on the knowledge about the objects in the scene (land, sea and clouds), which is used to partition the gray value histogram of the input image. Since clouds have been previously extracted, the obtained histogram is bimodal (land and sea classes), and the threshold can be set to the pixel value corresponding to the valley. The segmentation is not very sensitive to the threshold value selection, since, in most input images, the histogram is sparsely populated near the valley.

After region labeling [29], several land regions may appear. Depending on the cloud distributions, a single object (e.g., an island) may be split into various regions or even it may be completely covered and not appear in the partition. Therefore, detected land regions, that may not completely describe their associated objects, have to be matched with the objects in the reference image. Correspondences are estimated using a spatial coherency test relying on area values and centroid positions. The center of gravity of a given object $F_k(i,j)$ (kth object of a binary image F) is estimated using objects moments [29],

$$\overline{X}_{F_k} = \frac{\sum_i \sum_j j \cdot F_k(i,j)}{m_{00}} \quad \overline{Y}_{F_k} = \frac{\sum_i \sum_j i \cdot F_k(i,j)}{m_{00}} \tag{1}$$

where m_{00} represents the binary object area (zero-order moment). The same parameters are computed for the land regions detected in the input image.

The procedure sequentially compares each object from the reference image (R) with the land regions in the input image (S). Two tests of spatial coherence are conducted for each pair of land region and object. If a given pair fulfills both tests, the land region and the object are said to match and they are referred to as a *validated region* and a *validated object*, respectively:

1) *Euclidean distance test*:

$$\begin{aligned} & d\left(\left[\overline{X}_{R_i}, \overline{Y}_{R_i}\right], \left[\overline{X}_{S_j}, \overline{Y}_{S_j}\right]\right) \\ =& \text{Int}\left(\sqrt{\left(\overline{X}_{R_i} - \overline{X}_{S_j}\right)^2 + \left(\overline{Y}_{R_i} - \overline{Y}_{S_j}\right)^2}\right) \\ \leq& 25. \end{aligned} \tag{2}$$

2) *Area test*:

$$A(R_i, S_j) = \left(\frac{A_{S_j}}{A_{R_i}}\right) \cdot 100 \geq 50\%. \tag{3}$$

Threshold selections are based on the following considerations.

1) *Euclidean distance test:* This test handles situations where the maximum distance error between the reference and input images is greater than an expected threshold. This threshold is established by estimating the maximum

[2]General Bathymetric Chart of the Oceans. See http://www.ngdc.noaa.gov/mgg/gebco/gebco.html.

expected error in the satellite clock, a problem especially critical in AVHRR images [14], [18]. In NOAA AVHRR and SeaStar–SeaWiFS applications, 25 pixels correspond, approximately, to a distance of 27.5 km.

2) *Area test:* This test rejects situations where the region area rate is too small (e.g., less than 50%). Such situations are due to large zones occluded by clouds and do not yield suitable estimations of the centroid position.

Land regions in the input image that do not fulfill the spatial coherency tests are discarded.

Extraction of Reliable Edges: From the set of edges detected in the input image, those associated to actual sea–land transitions must be preserved to perform the contour matching. This process is carried out in two steps. First, all edges are estimated and, afterward, the reliable ones are detected. This way, the input image $I(x,y)$ is first convolved with a Sobel operator so initial edges are estimated. Estimated edges are used to define a gradient energy map as follows:

$$S(x,y) = -|\overline{\nabla I(x,y)}|^2 \tag{4}$$

where $\overline{\nabla I}$ is the gradient intensity normalized to [0,1].

The energy functional defined in (4) is negative, so those image points with lower values will correspond to higher gradients. Fig. 3 presents two examples of this procedure. Fig. 3(a) and (b) shows the input images, obtained using an orbital prediction model. Note that, particularly in Fig. 3(b), there are very few areas where the coastline is visible due to the cloud presence. Fig. 3(c) and (d) shows the gradient energy maps obtained from Fig. 3(a) and (b), respectively.

A morphological dilation is applied to the previously obtained binary cloud overlay $[M(x,y)]$ to solve possible misclassifications of isolated points

$$M \oplus B = \bigcup_{bi \in B} M_{bi} \tag{5}$$

where $\{B = b_1, b_2, \ldots, b_n\}$ is a binary mask containing n elements known as structuring elements, and $\oplus$ denotes the dilation operation of M by B [30].

The size of the selected structuring element has to be large enough to mask the maximum number of gradient pixels from the clouds outer contours and small enough to avoid the elimination of valid edge points of the desired areas. Experimental analyses with a large amount of images have shown that 5×5 is a suitable structuring element size for this application.

Once the cloud areas have been obtained, reliable edges are computed by masking the gradient energy map with the dilated cloud regions. Fig. 3(e) and (f) shows the respective cloud overlay. The edge classification into reliable and nonreliable ones is presented in Fig. 3(g) and (h).

To facilitate the convergence of the optimization algorithms (see Section III), estimated edges are smoothed by means of a Gaussian filter. The modified gradient energy map is defined by a 2-D convolution

$$E_{\text{edge}} = \{S(x,y) \cdot [M(x,y) \oplus B(x,y)]\} * G(x,y) \tag{6}$$

where $G(x,y)$ is a 2-D Gaussian function and masked pixels are eliminated from the convolution computation. Fig. 3(i) and (j) presents two different types of information: the estimated edges that have been selected as reliable from the input image and the reference contours for this scene. Reference contours have been superimposed to the reliable edges for comparison purposes. Observe, particularly in Fig. 3(j), that due to the presence of clouds the process may retain very few edges as reliable information.

III. Contour-Matching Approaches

Two automatic contour-matching procedures are described in this section. In both techniques, we have assumed that the relationship between the input image, obtained from the orbital prediction model, and the reference image can be expressed by a 2-D affine transformation [1], [23], since the systematic errors have been previously compensated by the Kepplerian model.

For the considered affine transformation model, we can write for each pair of related points

$$X_O = [1 \quad X_I \quad Y_I] \begin{bmatrix} a_0 \\ a_1 \\ a_2 \end{bmatrix} \quad Y_O = [1 \quad X_I \quad Y_I] \begin{bmatrix} b_0 \\ b_1 \\ b_2 \end{bmatrix} \tag{7}$$

where (X_O, Y_O), (X_I, Y_I) are, respectively, the initial and final positions of a contour point and $\{a_0,\ a_1,\ a_2\}$, $\{b_0,\ b_1,\ b_2\}$ are the transformation parameters. The six transformation parameters are estimated using all pairs of accepted points (N), through a minimum squares solution

$$\hat{X} = (W^T W)^{-1}(W^T R_X);\ \hat{Y} = (W^T W)^{-1}(W^T R_Y) \tag{8}$$

where

$$W = \begin{bmatrix} 1 & X_{I_1} & Y_{I_1} \\ \cdots & \cdots & \cdots \\ 1 & X_{I_N} & Y_{I_N} \end{bmatrix} \quad R_X = \begin{bmatrix} X_{O_1} \\ \vdots \\ X_{O_N} \end{bmatrix} \quad R_Y = \begin{bmatrix} Y_{O_1} \\ \vdots \\ Y_{O_N} \end{bmatrix} \tag{9}$$

and

$$\hat{X} = \begin{bmatrix} A_X \\ B_X \\ C_X \end{bmatrix} \quad \hat{Y} = \begin{bmatrix} A_Y \\ B_Y \\ C_Y \end{bmatrix}. \tag{10}$$

Finally, the input image is transformed using the following correction function:

$$\begin{bmatrix} X_I \\ Y_I \end{bmatrix} = \begin{pmatrix} A_X & B_X \\ A_Y & B_Y \end{pmatrix} \cdot \begin{bmatrix} X_o \\ Y_o \end{bmatrix} + \begin{pmatrix} C_X \\ C_Y \end{pmatrix}. \tag{11}$$

The 2-D affine parameters will allow an accurate image georeferencing. They can be obtained as a final approximation of a set of local optimizations (e.g., by means of a bilinear regression) or directly as the result of a global optimization. In this section, both approaches are considered.

Both contour-matching approaches are iterative energy minimization processes, which start from an initial estimate. If a contour is initially placed too far from its correct position, the convergence may be slow or even erroneous. So, contour positions are initialized to allow a faster and more reliable convergence. Usually, initialization is application

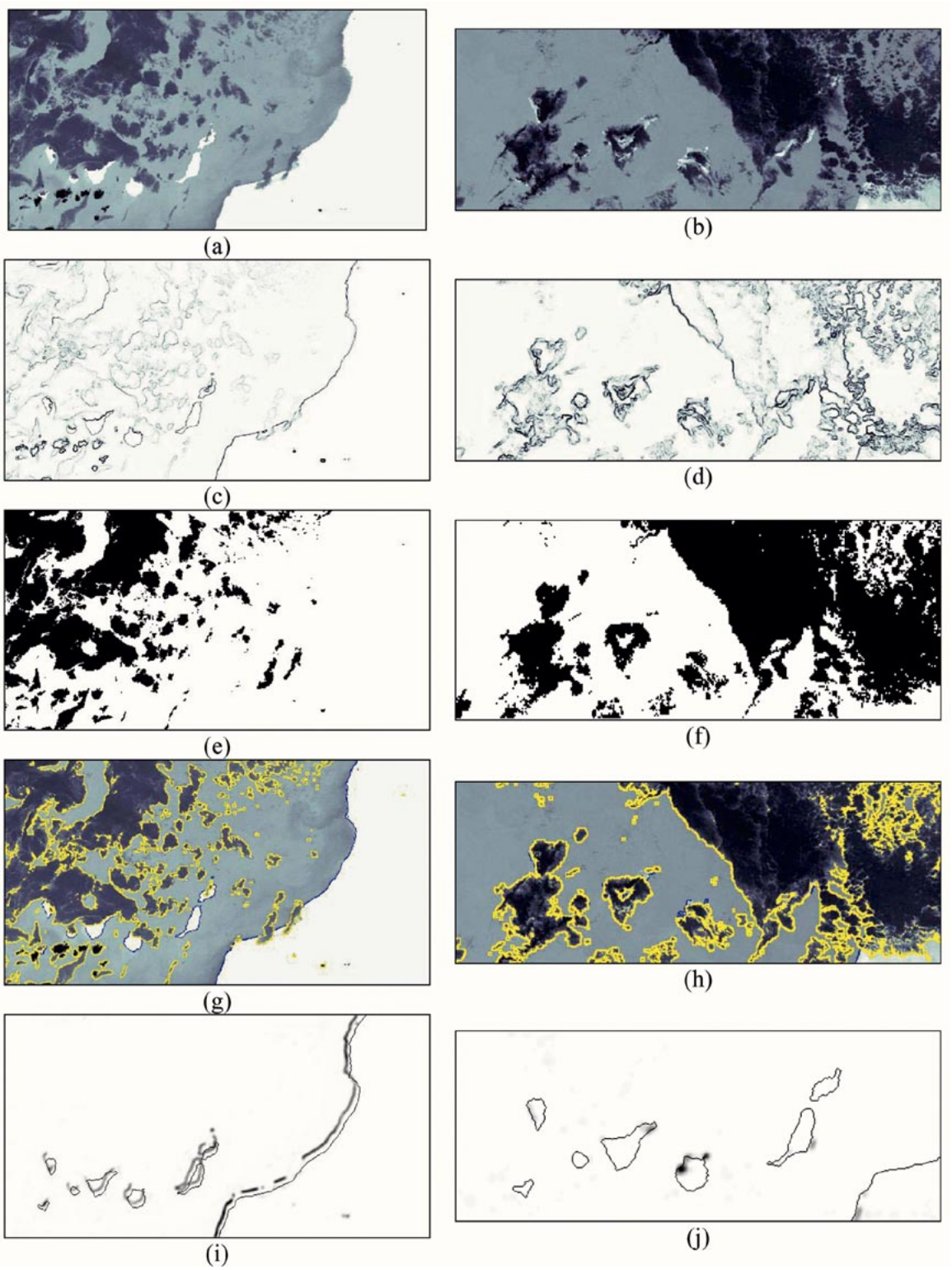

Fig. 3. Examples of feature extraction from NOAA AVHRR images. (a), (b) Input images. (c), (d) Gradient energy maps. (e), (f) Cloud overlays. (g), (h) Classification of the useful (blue contour) and useless (yellow contour) pixels. (i), (j) Smoothed gradient energy maps of reliable areas.

specific, requiring either prior knowledge of the problem or user interaction. In our case, the initialization only performs a uniform translation of the reference contours on the input image. Furthermore, different initialization strategies are required, depending on the contour optimization technique to be used.

A. Local Optimization Approach

The proposed minimization algorithm allows a contour to converge in an iterative way on an area of high-magnitude image energy: in this case, edges. In the local optimization approach, convergence is performed separately for each object and so is the initialization strategy. Contours are initialized by aligning

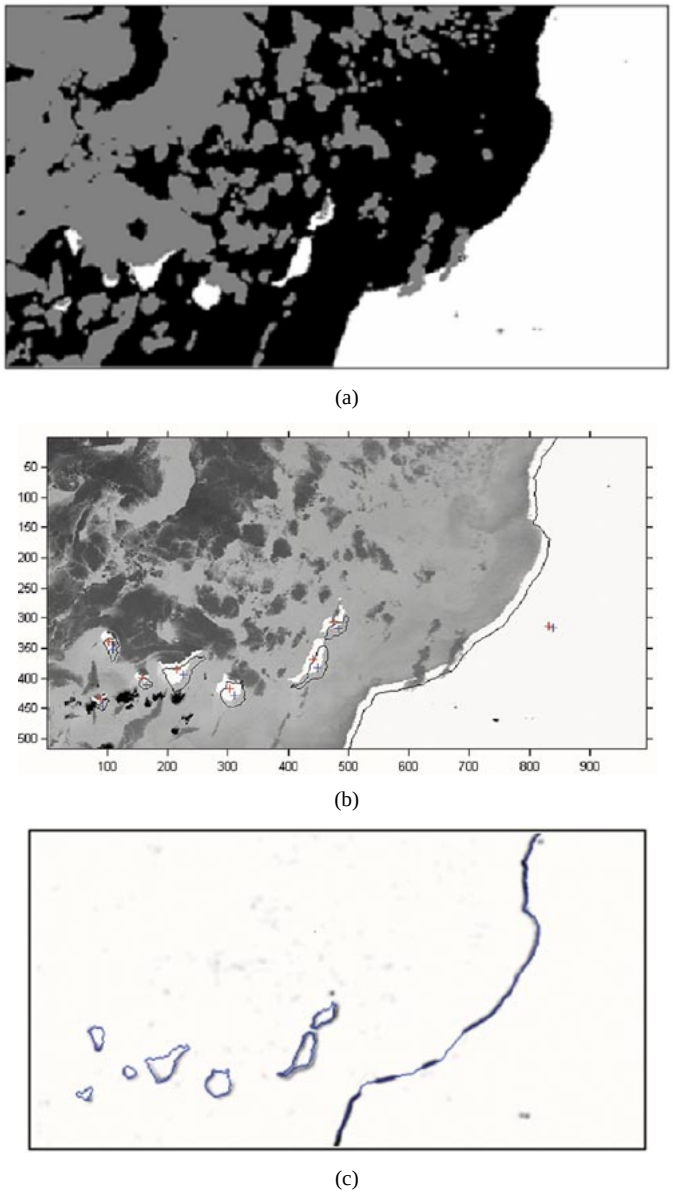

Fig. 4. Contour position initialization. (a) Segmented image: land (white), clouds (gray), and sea (black) pixels. (b) Centroids position. In the cross pairs, the blue cross is in the reference image, and the red cross is in the input image. (c) Results of contours position initialization (blue) on smoothed gradient energy map.

the gravity centers of each validated region in the input image and of the corresponding object in the reference image. An example of the results from the local initialization stage is shown in Fig. 4. Fig. 4(a) presents the segmentation of the image in Fig. 3(a). In turn, Fig. 4(b) presents the centroid positions on the reference and input images, whereas the contours positions obtained using the local initialization are shown in Fig. 4(c).

After contour initialization, each object is handled separately. Given a reference image with m objects, let us analyze the optimization of an object i (e.g., an island) whose contour has n_i points. Let $\nu_i^{(k)} = \{\nu_{ij}^{(k)} | j = 1, 2, \ldots, n_i\}$ be the contour of the ith object after the kth iteration. Its total energy is

$$E_{\text{contour}_i}^{(k)} = E_{\text{contour}}(\nu_i^{(k)}) = \sum_{j=1}^{n_i} E_{\text{edge}}(\nu_{ij}^{(k)}) \qquad (12)$$

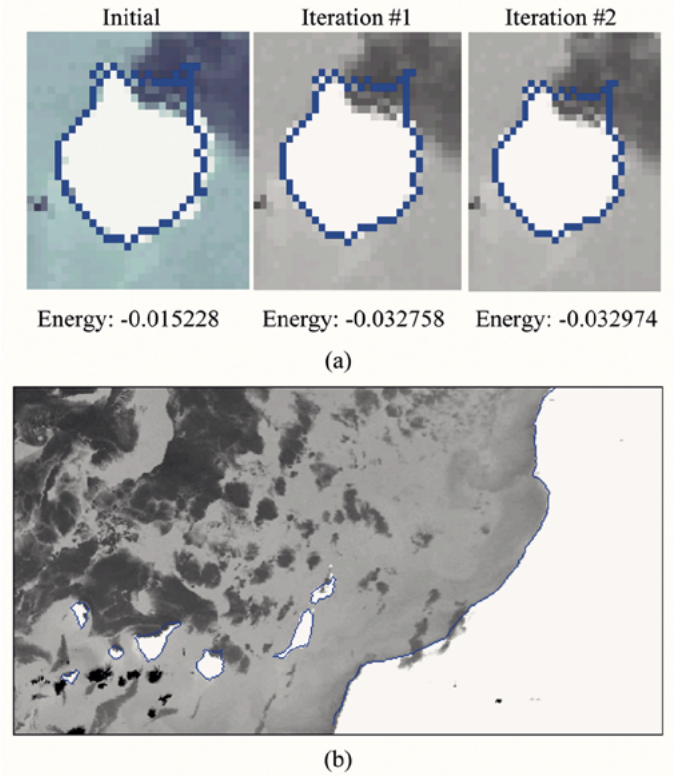

Fig. 5. Example of the iterative energy minimization process. (a) For a given validated region and (b) for the whole set of validated regions.

where $E_{\text{edge}}(\cdot)$ is the energy of one point of the contour evaluated over the gradient energy map [see (6)].

The algorithm allows uniform translations $d = \{d_x, d_y\}$ in a neighborhood (typically 5×5 pixels) centered at the current position. Every site in this neighborhood is a candidate point for updating, i.e., a one-pixel quantization step is used. The algorithm moves $\nu_i^{(k)}$ to a new location $\nu_i^{(k+1)}$ according to the following updating rule

$$\nu_i^{(k+1)} = \arg\min_d E_{\text{contour}}(\nu_i^{(k)}). \qquad (13)$$

This way, at each iteration, an exhaustive search is carried out, looking for the reference contour position leading to the minimum energy. The process is iterated reducing, at each iteration, 1) the smoothing degree and the amplitude of the gradient energy map of the reliable areas (see Section II) and 2) the search window size. When two successive iterations lead to the same minimum energy the process ends. This process is performed for all validated reference objects.

Fig. 5 shows the result of the local contour optimization applied to the NOAA AVHRR image of Fig. 3(a). Fig. 5(a) presents the iterative energy minimization for a validated region from Fig. 3(a), whereas Fig. 5(b) shows the result for the whole set of validated regions.

The affine transformation parameters are estimated based on the final positions of the reference contours. To improve the estimation robustness, all final reference contours must pass a local consistency test. A reference contour is accepted only if enough points from its final version overlap reliable edges. Typically, a

contour is accepted if more than 10% of its points overlap reliable edges.

Least Square Fitting: It consists of computing a bilinear regression from the initial and final positions for each of the points of the accepted contours (11). Nearest neighbor resampling is applied for gray-level interpolation. This procedure is globally performed, so the positions of those parts of land that could not be detected in the contour-matching process are now estimated.

B. Global Optimization Approach

The global optimization approach is based on the simultaneous optimization of all reference contours on the energy map gradients of the input image. Therefore, the initialization strategy will simultaneously shift all the reference contours. The horizontal and vertical translation parameters defining the contour initialization are computed using different approaches, given the different nature of the errors in both directions. The horizontal displacement is, essentially, due to inaccuracies in the orbital model, in the satellite ephemeris data, and nonzero values for the roll of the spacecraft. Therefore, the horizontal translation suffered by each object is different and an average value is adopted. In turn, the vertical displacement is, mainly, due to the satellite clock drift and nonzero value for the spacecraft's pitch. Hence, all objects suffered, approximately, the same vertical displacement and that of the largest validated region is assumed.

In the global optimization, the six-dimensional (6-D) space defining the set of possible affine transformations

$$\partial = \{A_X, B_X, C_X, A_Y, B_Y, C_Y\} \tag{14}$$

is analyzed looking for the solution leading to the lowest energy. At first, the translation parameters provided by the contour initialization are used as initial guess of a first-order bivariate polynomial transformation (11).

Multidimensional Global Search: It is based on the transformed contour image and works on the affine transformation parameters domain. Given an initial point in the 6-D space, its neighborhood is defined by limiting and quantizing the range of possible values of each affine transformation parameter $\{A_X, B_X, C_X, A_Y, B_Y, C_Y\}$. The point in the 6-D neighborhood leading to the minimum energy is selected

$$\begin{aligned} E_{\text{global}}^{(k)} &= \arg\min_{\partial} \sum_{i=1}^{m} E_{\text{contour}_i}^{(k)} \\ &= \arg\min_{\partial} \sum_{i=1}^{m} \sum_{j=1}^{n_i} E_{\text{edge}}(\nu_{ij}^{(k)}) < E_{\text{global}}^{(k-1)} \end{aligned} \tag{15}$$

where m is the set of objects, n_i is the number of contour points of object i and $E_{\text{edge}}(\cdot)$ is the energy of one point of the contour evaluated over the gradient energy map [see (6)] after the kth iteration.

If the new contour position reduces the global energy, the process is iterated using the selected point as center of the new 6-D neighborhood. At each iteration, the contour positions are updated

$$\begin{aligned} \begin{bmatrix} x^{(k)} \\ y^{(k)} \end{bmatrix} &= \begin{pmatrix} A_X^{(k)} & B_X^{(k)} \\ A_Y^{(k)} & B_Y^{(k)} \end{pmatrix} \begin{pmatrix} A_X^{(k-1)} & B_X^{(k-1)} \\ A_Y^{(k-1)} & B_Y^{(k-1)} \end{pmatrix} \cdot \begin{bmatrix} x^{(k-1)} \\ y^{(k-1)} \end{bmatrix} \\ &\quad + \begin{pmatrix} A_X^{(k)} & B_X^{(k)} \\ A_Y^{(k)} & B_Y^{(k)} \end{pmatrix} \begin{pmatrix} C_X^{(k-1)} \\ C_Y^{(k-1)} \end{pmatrix} + \begin{pmatrix} C_X^{(k)} \\ C_Y^{(k)} \end{pmatrix}. \end{aligned} \tag{16}$$

The global search is performed in a 6-D space that is structured. Therefore, heuristic algorithms [31] can be applied to efficiently exploit this characteristic and avoid the exhaustive exploration of the search space.

Based on the analysis of the nature of the problem, the sensitivity study of the energy function for each parameter and the parameters correlation, the following strategies are adopted.

1) *Set limits to the solution space for each parameter.* Residual errors, after geometric corrections (orbital prediction model) and contours initialization, require moderate affine parameters values (e.g., translations lower than five pixels). Therefore, the search space can be restricted to a small neighborhood.
2) *Discretize the solution space.* Although the energy function is multimodal, the spare presence of maxima in a small neighborhood allows a multiresolution analysis of the search space. Therefore, at each iteration, the search space is finer sampled around the previous solution.
3) *Exploration strategy.* Given the good behavior of the energy function, each dimension (parameter) of the problem is separately searched following a conjugate gradient strategy [32].

Based on the obtained correction function (11), the input image is transformed and resampled using nearest neighbor interpolation. Fig. 6 presents the iterative process of the global optimization on the image of Fig. 3(a) after contour initialization. For each iteration, the initial/final energy values are provided.

C. Combined Method

As it will be shown in Section V, the global optimization approach, although being more robust than the local one, may converge to solutions with higher energy values than the solution obtained by the local one. This occurs when the initial solution in the global optimization approach is too far away from the local minimum so that the heuristic approach and the discretization strategy cannot ensure a correct convergence.

In the combined method, the global optimization approach is initialized using the result of the local optimization technique [33]. That is, the initial affine parameters are computed using the solution of expression (11). In consequence, they are very close to the optimal solution. The combined method, not only leads to a more reliable technique, but it also is computationally more efficient than the global optimization approach.

IV. Georeferencing Accuracy Estimation Technique

A common procedure to assess the quality of the georeferenced image is to compute the error in the location of a few

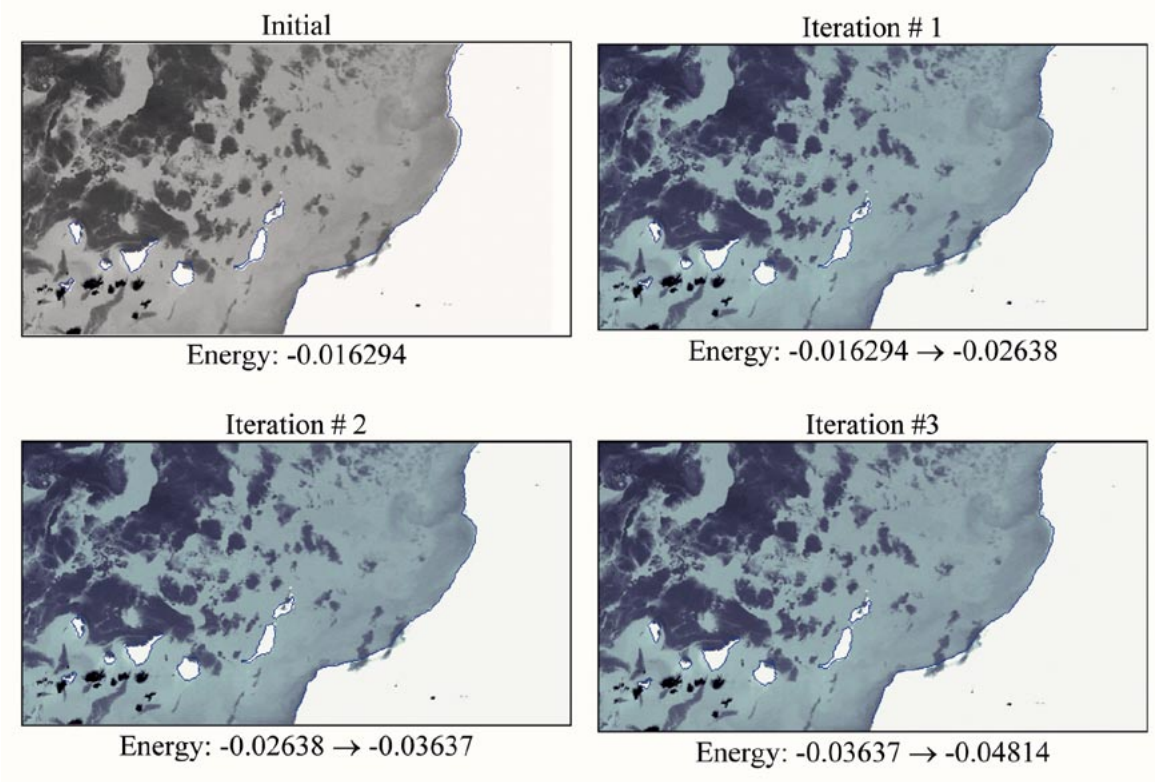

Fig. 6. Sequence showing the convergence of the contours to the desired optimal positions, using the global optimization approach.

Fig. 7. Error field generated for a reference image.

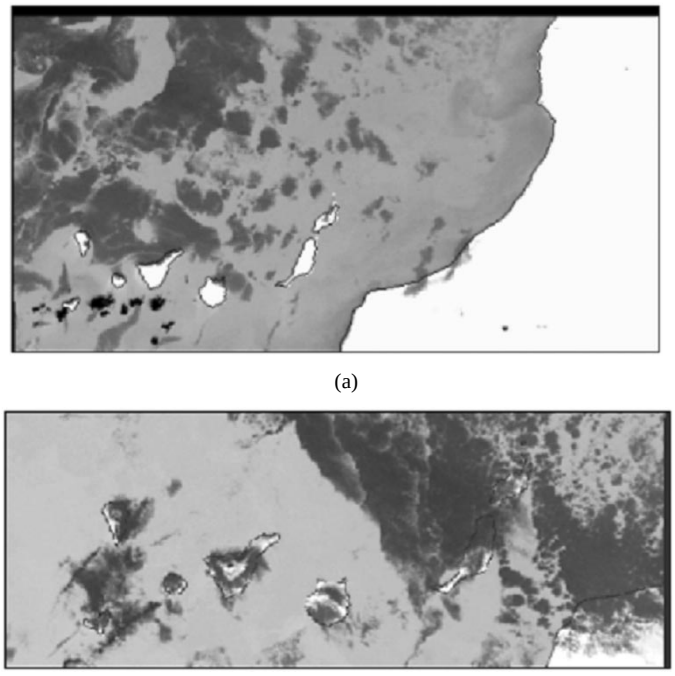

(a)

(b)

Fig. 8. Georeferencing results of SST data. (a) Image of July 3, 1998 (517×993) processed using the local optimization approach. (b) Image of January 9, 1997 (237×629) processed using the global optimization approach.

control points. As it has been commented in Section I, this procedure is subject to problems of availability and representativity of such points as well as uncertainty in their interactive location. To overcome these problems, a new method has been developed based on the use of all the image available information. This way, the distance between the reference contours and the transformed reliable edges (see Section II) is computed. The procedure has two parts.

A. Error Field Generation

A distance map is generated computing those pixels which are at a given distance from the reference contours. In this implementation, distances are computed by successive dilations of the reference contours. Fig. 7 shows an example of the error field obtained from a reference image (see Fig. 2). Distance values greater than 3 are not computed because errors of such magnitude do not appear after the geometric correction of the residual errors.

B. Extraction of Sea–Land Contours

The reliable outer land-sea contours are extracted and transformed by the obtained correction function, to superimpose them on the distance map. Contours are extracted from the gradient map of the relevant areas. In this application, we have used a thresholding approach given its simplicity. Since gradients are smooth, the resulting contours have to be thinned up to one pixel width.

Finally, the distance map [DM(.)] is evaluated at all points (p) belonging to the binary representation of the transformed contours (C). The final RMS error is computed by adding up these values and normalizing them by the total number of contour points in C ($N = |C|$)

$$\mathrm{RMSE} = \sqrt{\frac{\sum_{p \subset C} \mathrm{DM}(p)}{N}}. \tag{17}$$

As it will be shown in the following section, this method enables the use of a large number of points in the RMS error computation, making the measure more robust.

V. Experimental Results

In this section, we provide some experimental results for single sensor and multisensor image georeferencing using the previous automatic contour-matching algorithms.

The proposed algorithms have been tested in a large set of satellite images. Here we present a subset that illustrates some of their relevant features. Fig. 8 shows the results obtained for the NOAA-14 AVHRR images of Fig. 3(a) and (b). Qualitatively, the correspondence between the reference and input images obtained by the proposed algorithms is accurate to within a pixel error in average. Fig. 9(a) and (b) shows the results achieved by the proposed contour-matching technique applied to a NOAA-14 AVHRR image of the Mediterranean area and a SeaStar–SeaWiFS image of the Canary Island area. Note that both examples contain portions with partial and total occlusions. The results present accurate estimations of the location of all regions (even the nonvisible ones). It is worth mentioning that images in Figs. 8(b) and 9(b) can only be successfully georeferenced with high precision using the global optimization approach due to the presence of large occluded areas. Contours in such images will not pass the local consistency test included in the local optimization technique, disabling, in consequence, its use.

The results in Fig. 9 allow assessing the robustness of the proposed technique, since they have been obtained using different orbital prediction models to provide first-guess earth location. While the NOAA AVHRR examples have been processed using the *ad hoc* algorithm presented in [34], the different processing levels applied to the SeaWiFS data are included in the SeaDAS (SeaWiFS Data Analysis System) software package. This package was developed under the NASA oceanographic biochemistry program [13] and made available for research centers and associated users within the framework of the *SeaWiFS Project*, in which our receiving ground station (HCAN) is an active part.

TABLE I
Results of Satellite Image Georeferencing for Five Test Cases

Image Satellite	Method	Initial Energy	Final Energy	R.M.S.
18 January 1998 NOAA 14	Local	- 0.0295	-0.0635	1.135
	Global		-0.0603	1.297
	Combined		-0.0739	0.768
3 July 1998 NOAA 14	Local	-0.0155	-0.0537	0.987
	Global		-0.0488	1.143
	Combined		-0.0562	0.762
24 April 1999 NOAA 14	Local	- 0.0163	-0.0545	1.275
	Global		-0.0527	1.427
	Combined		-0.0613	0.857
24 April 1999 SEASTAR	Local	- 0.0466	-0.0793	1.015
	Global		-0.0705	1.187
	Combined		-0.0925	0.695
15 September 2000 SEASTAR	Local	-0.0142	-0.0269	1.094
	Global		-0.0257	1.272
	Combined		-0.0281	0.899

TABLE II
Comparison Between an Area-Based Technique and the Proposed Algorithm

Image	Area-based technique	Local Optimization technique
12 October 1997	**n** 7 **x** 1.5404 **y** 2.1042	**n** 1603 **x** 1.2934 **y** 0.8028
28 November 1999	**n** 4 **x** 1.9672 **y** 1.8477	**n** 798 **x** 0.5613 **y** 0.3561
3 January 2000	**n** 7 **x** 1.2754 **y** 1.5583	**n** 1910 **x** 0.5401 **y** 0.5631

TABLE III
Extrapolation of Transformation Functions, Evaluated Over Three Test Cases

Image	Zone	RMSE (Nº points)
5 June 1998	Zone 1: Canary I. 27-32ºN, 9-19ºW	**1 :** 0.84957 (1506) **1 → 2 :** 1.82867 (901)
	Zone 2: Gibraltar 33-37ºN, 3-10ºW	**2 :** 0.88428 (901) **2 → 1 :** 1.89258 (1506)
11 June 1998	Zone 1: Canary I. 27-32ºN, 9-19ºW	**1 :** 1.00056 (895) **1 → 2 :** 3.22235 (725)
	Zone 2: Gibraltar 33-37ºN, 3-10ºW	**2 :** 1.11604 (725) **2 → 1 :** 2.38967 (895)
28 November 1999	Zone 1: Canary I. 27-32ºN, 9-19ºW	**1 :** 1.08958 (1546) **1 → 2 :** 3.17302 (1855)
	Zone 2: Gibraltar 33-37ºN, 3-10ºW	**2 :** 0.89503 (1855) **2 → 1 :** 3.34498 (1546)

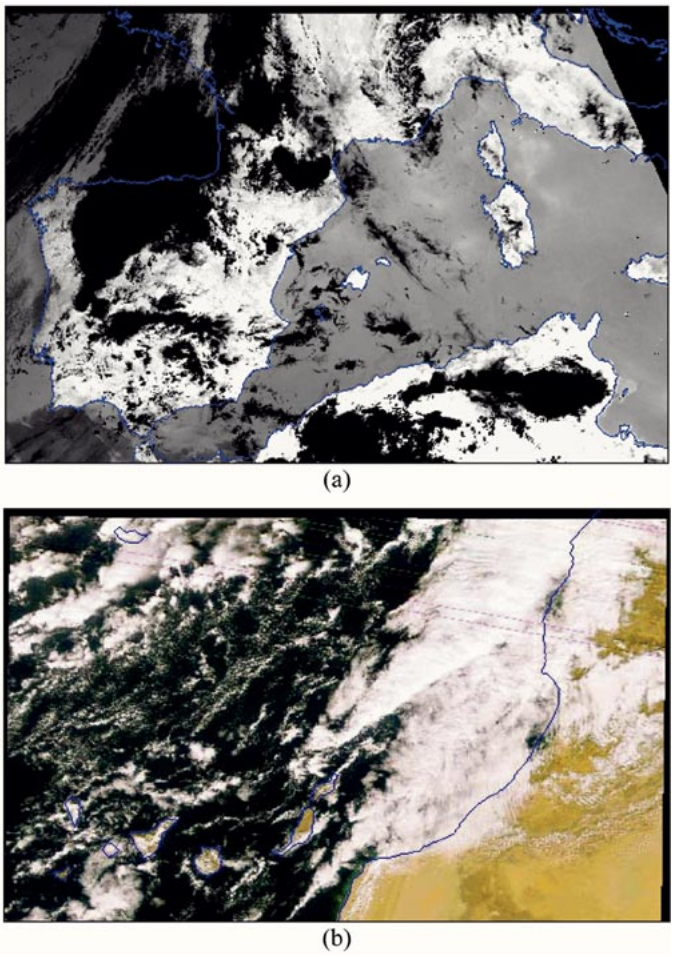

Fig. 9. Georeferencing results of NOAA-14 AVHRR and SeaStar SeaWiFS imagery. (a) Image of May 16, 2000 (1358 × 1981) processed using the local optimization approach. (b) Image of January 16, 2000 (618 × 993) processed using the global optimization approach.

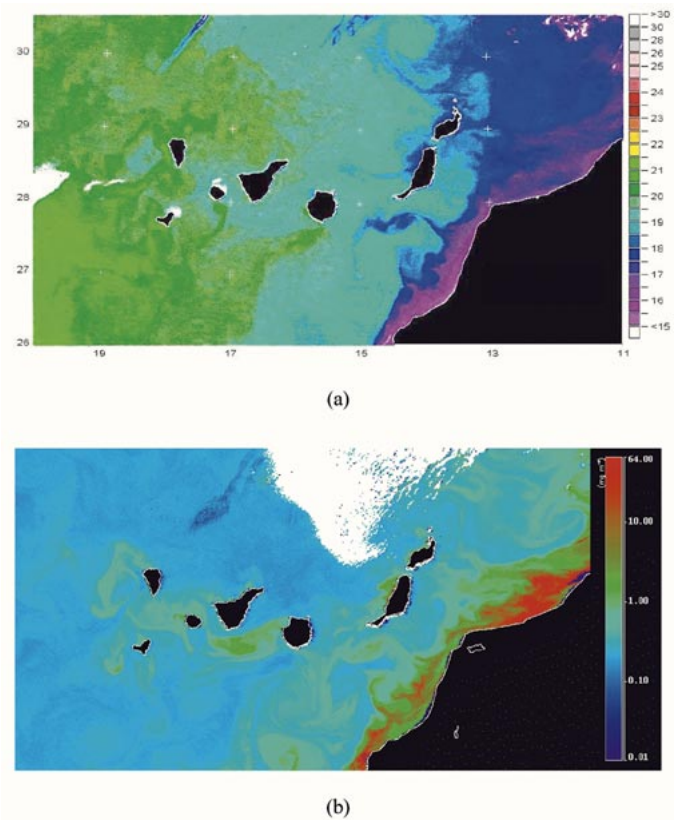

Fig. 10. Results of contour-matching approach of multisensor images of April 24, 1999, georeferenced into the Mercator projection. (a) SST image from NOAA-14 AVHRR and (b) Ocean color image from SeaStar–SeaWiFS.

Table I shows the results obtained in a subset of NOAA-14 AVHRR and SeaStar–SeaWiFS images. In it, the captured data and the initial/final energy obtained in the minimization process are presented for the three proposed algorithms. In all cases, images present few occluded areas and therefore the local optimization scheme presents higher accuracy (around 10%) than the global one. In turn, the combination of both methods outperforms their isolated application.

From the perspective of the analysis and extraction of conclusions, two particular cases are presented which give an idea of the limits of the proposed technique. The first case corresponds to the comparison between the proposed optimization techniques with the area-based approaches, as implemented in [25]. Results are presented in Table II detailing the number of points used in the transformation parameters estimation (n) and the total RMS error in the horizontal (x) and vertical (y) directions. The proposed algorithm outperforms area-based techniques by over half a pixel on the average, even when a large number of control points are available. In consequence, these algorithms are adequate for automatic georeferencing satellite images, even when they have partial or total occlusions and, thus, it is difficult to obtain a large number of well-distributed GCPs.

The second case evaluates the error when extrapolating the transformation functions from a specific region to a different one in the same image. This is a common situation in oceanographic studies in which coast lines may be gathered in a small area of the image, while, relevant oceanographic structures may be present far away from this area. To be able to quantify the error in such cases, images containing coastlines in different areas are used. Three cases are presented in Table III. For each image, the first row shows the results when using the Canary Islands area to compute the transformation functions which are extrapolated over the Gibraltar area. The accuracy of the extrapolation is assessed in this last area. The second row presents the inverse situation. Results show that high precision is not achieved, exhibing maximum errors of three pixels. This circumstance is due to the fact that the transformation functions depend on the region where the coefficients were obtained and on its location with respect to the satellite track.

Finally, Fig. 10 presents the results of the proposed method in multisensor images, corresponding to sea surface temperature and ocean color data, acquired by the AVHRR and SeaWiFS sensors respectively. In Fig. 10, the correspondence between the reference and input images shows that the georeferencing obtained by the proposed algorithms is accurate to within a pixel error in average (Table I).

Our algorithm is reasonably efficient in terms of computational complexity. The creation of typical 517×993 (1041×1356) high-precision AVHRR (SeaWiFS) georeferenced images requires approximately 110 (325) s of

TABLE IV
AVERAGE PERCENTAGES OF COMPUTATIONAL LOAD REQUIRED FOR EACH PART OF THE COMPLETE SYSTEM

Image AVHRR (517 × 993)	Feature Extraction		Feature Correspondence	
	Extraction of reference contours	Extraction of validated regions	Contour position initialization	Contour matching approach
Local optimization	1.3 %	12.3 %	24.7 %	61.7 %
Global optimization	0.9 %	9.4 %	14.2 %	75.5 %

computational load, on an IBM IntelliStation ZPro computer. In addition, it is important to highlight two aspects. First, the type of geometric processing we are handling is not usually required in real time, except during the oceanographic campaigns, and second, the fact that the algorithms have not been fully optimized. In spite of that, and as approximate information, Table IV includes the respective percentages of computational load required for each part of the complete system.

VI. CONCLUSION

This paper has dealt with automatic georeferencing of remotely sensed imagery. This procedure appears often in the processing of multitemporal and/or multisensor image analysis, such as multisource data fusion, multitemporal change detection, and validation of satellite data using *in situ* field measurements. In this work, we have explored the critical elements for an automated image georeferencing system using NOAA AVHRR and SeaStar–SeaWiFS imagery, which are first coarsely georeferenced using an orbital prediction model. These elements include feature extraction, contour initialization and contour optimization.

For this last process, we developed two contour-matching techniques, based on a general affine transformation, which model directly the corrections in the image domain without an explicit identification of the distortion sources. The local optimization scheme achieves slightly higher accuracy (around 10%) with respect to the multidimensional global optimization scheme (Table I). However, it is less robust in the presence of large partial or total occluded land areas, due to the local consistency test restrictions. Furthermore, to achieve subpixel accuracy, both methods have been combined. In this case, a double transformation is performed and, in consequence, the final search is carried out in an area very close to the optimum solution.

Several experimental results for single sensor image georeferencing from different geographic areas and multisensor image georeferencing (AVHRR versus SeaWiFS) have verified the robustness and accuracy of the proposed algorithms, regardless the initial orbital prediction model, demonstrating their capability of georeferencing satellite images within one pixel. Furthermore, a new technique has been proposed to assess the accuracy of georeferencing approaches, which makes use of all reliable information in the image.

In summary, the proposed technique improves the analysis and data interpretation accuracy and facilitates its update to future remote sensing sensors or other applications: multitemporal classification, multisensor data fusion, structures recognition and tracking, etc. Currently, and exploiting its modularity, it has been improved with a friendly graphical user interface, and it is being used at the University of Las Palmas to produce 1-km resolution sea surface temperature and high phytoplankton concentrations maps [35].

The favorable results from this study have spawned a follow-up project that consists of the upgrade of the developed techniques to automatic registration of any multisensor images, e.g., TERRA-MODIS and ATSR-ERS.

ACKNOWLEDGMENT

The authors would like to express special gratitude to J. Marcello (ULPGC) for his help and support and to P. Salembier, M. Pardàs (UPC), and the anonymous reviewers for their constructive comments and suggestions.

REFERENCES

[1] R. A. Schowengerdt, *Remote Sensing: Models and Methods for Image Processing*, 2nd ed. New York: Academic, 1997.
[2] D. A. Mouat, G. G. Mahin, and J. Lancaster, "Remote sensing techniques in the analysis of change detection," *Geocarto Int.*, vol. 2, pp. 39–50, 1993.
[3] C. Pohl and J. L. Van Genderen, "Multisensor image fusion in remote sensing: Concepts, methods and applications," *Int. J. Remote Sens.*, vol. 19, pp. 823–854, 1998.
[4] R. Haralick and L. Shapiro, *Computer and Robot Vision*. Reading, MA: Addison-Wesley, 1993, vol. 2.
[5] J. Flusser and T. Suk, "A moment-based approach to registration of images with affine geometric distortion," *IEEE Trans. Geosci. Remote Sensing*, vol. 32, pp. 382–387, Mar. 1994.
[6] H. Li, B. S. Manjunath, and S. K. Mitra, "A contour-based approach to multisensor image registration," *IEEE Trans. Image Processing*, vol. 4, pp. 320–334, Mar. 1995.
[7] L. M. G. Fonseca and B. S. Manjunath, "Registration techniques for multisensor remotely sensed imagery," *Photogramm. Eng. Remote Sens.*, vol. 562, pp. 1049–1056, 1996.
[8] X. Dai and S. Korran, "A feature-based image registration algorithm using improved chain-code representation combined with invariant moments," *IEEE Trans. Geosci. Remote Sensing*, vol. 37, pp. 2351–2362, Sept. 1999.
[9] Z. Mao, D. Pan, H. Huang, and W. Huang, "Automatic registration of SeaWiFS and AVHRR imagery," *Int. J. Remote Sens.*, vol. 22, pp. 1725–1735, 2001.

[10] H. S. Stone and R. Wolpov, "Blind cross-spectral image registration using prefiltering and fourier-based translation detection," *IEEE Trans. Geosci. Remote Sensing*, vol. 40, pp. 637–650, Mar. 2002.
[11] J. Le Moigne, W. J. Campbell, and R. F. Cromp, "An automated parallel image registration technique based on the correlation of wavelet features," *IEEE Trans. Geosci. Remote Sensing*, vol. 40, pp. 1849–1864, Aug. 2002.
[12] A. P. Cracknell, *The Advanced Very High Resolution Radiometer*. New York: Taylor & Francis, 1997.
[13] C. R. McClain and K. Arrigo, "SeaWiFS Data Analysis System," NASA, Greenbelt, MD, NASA Tech. Memo. UPN S79–11–03–20, 1996.
[14] G. D'Souza, A. S. Belward, and J.-P. Malingreau, *Advances in the Use of NOAA-AVHRR Data for Land Applications*. Amsterdam, The Netherlands: Kluwer, 1996.
[15] W. J. Emery, J. Brown, and Z. Paul Nowack, "AVHRR image navigation: Summary and review," *Photogramm. Eng. Remote Sens.*, vol. 55, pp. 1175–1183, 1989.
[16] A. Marsouin and P. Brunel, "Navigation of AVHRR images using Argos or TBUS bulletins," *Int. J. Remote Sens.*, vol. 12, pp. 1575–1592, 1991.
[17] J. A. Richards, *Remote Sensing Digital Image Analysis—An Introduction*, 2nd ed. Berlin: Springer-Verlag, 1993.
[18] V. M. Krasnopolsky and D. Breaker, "The problem of AVHRR image navigation revisited," *Int. J. Remote Sens.*, vol. 15, pp. 979–1008, 1994.
[19] J. F. Moreno and F. Meliá, "A method for accurate geometric correction of NOAA AVHRR HRPT data," *IEEE Trans. Geosci. Remote Sensing*, vol. 31, pp. 204–226, Jan. 1993.
[20] G. W. Rosborough, D. Baldwin, and W. J. Emery, "Precise AVHRR image navigation," *IEEE Trans. Geosci. Remote Sensing*, vol. 32, pp. 644–657, May 1994.
[21] M. Bachmann and J. Bendix, "An improved algorithm for NOAA-AVHRR image referencing," *Int. J. Remote Sens.*, vol. 13, pp. 3205–3215, 1992.
[22] D. Ho and A. Asem, "NOAA AVHRR image referencing," *Int. J. Remote Sens.*, vol. 7, pp. 895–904, 1986.
[23] P. Illera, J. A. Delgado, and A. Calle, "A navigation algorithm for satellite images," *Int. J. Remote Sens.*, vol. 17, pp. 577–588, 1996.
[24] P. Bordes, P. Brunel, and A. Marsouin, "Automatic adjustment of AVHRR navigation," *J. Atmos. Ocean. Technol.*, vol. 9, pp. 15–27, 1992.
[25] F. Eugenio, J. Marcello, A. Hernández-Guerra, and E. Rovaris, "Methodology to obtain accurate sea surface temperature from locally received NOAA-14 data in the Canary-Azores-Gibraltar area," *Sci. Marina*, vol. 65, pp. 127–137, 2001.
[26] F. S. Patt, R. H. Woodward, and W. W. Gregg, "An automated method for navigation assessment for earth survey sensors using island targets," *Int. J. Remote Sens.*, vol. 18, pp. 3311–3336, 1997.
[27] D. E. Anderson *et al.*, *World Data Bank II: Content, Structure and Applications*. Washington, DC: Central Intelligence Agency, Office of Geographic and Cartographic Res., 1973.
[28] P. W. Saunders and K. T. Kriebel, "An improved method for detecting clear sky radiances from AVHRR data," *Int. J. Remote Sens.*, vol. 9, pp. 123–150, 1988.
[29] R. Jain, R. Kasturi, and B. G. Schunck, *Machine Vision*. New York: McGraw-Hill, 1995.
[30] J. Serra, *Image Analysis and Mathematical Morphology*. New York: Academic, 1997.
[31] C. R. Reeves, *Modern Heuristics Techniques for Combinatorial Problems*. New York: McGraw-Hill, 1995.
[32] D. G. Luenberger, *Optimization by Vector Space Methods*. New York: Wiley, 1969.
[33] F. Eugenio, F. Marqués, and J. Marcello, "Pixel and sub-pixel accuracy in satellite image georeferencing using an automatic contour matching approach," in *Proc. IEEE Int. Conf. Image Processing*, Oct. 2001, pp. I.822–I.825.
[34] F. Eugenio, J. Marcello, and A. Hernández-Guerra, "Improvements on the methodology to obtain accurate and automatic maps of sea surface temperature from NOAA-AVHRR data," in *Proc. IGARSS*, vol. V, July 2000, pp. 1827–1829.
[35] F. Eugenio, J. Marcello, F. Marqués, A. Hernández-Guerra, and E. Rovaris, "A real-time automatic acquisition, processing and distribution system for AVHRR and SeaWiFS imagery," *IEEE Geosci. Remote Sensing Newslett.*, no. 120, pp. 10–15, Sept. 2001.

Francisco Eugenio (M'00–A'00) was born in Las Palmas, Spain, in 1964. He received the B.S., M.S., and Ph.D. degrees from the University of Las Palmas of Gran Canaria (ULPGC), Las Palmas, Spain, in 1993 and 2000, respectively, both in electrical engineering.

He joined the Department of Signal and Communications, ULPGC, in June 1996. From 1998 to December 2000, he was with the Technical University of Catalunya in Barcelona (UPC), Barcelona, Spain, in the image processing group. Since 2003, he is an Associate Professor at ULPGC, having served as Associate Dean of the Telecommunication School (EUITT) at ULPGC (1994–1999). He is currently lecturing on the area of remote sensing and radar. His current research interests include remote sensing image processing, modeling, and georeferencing, especially in applied remote sensing in the field of physical oceanography. In these areas, he is author or coauthor of many publications that have appeared as journal papers and proceeding articles. His most recent research focuses on new methodological developments for automatic registration and fusion of multisensor/multiresolution satellite image data.

Ferran Marqués (S'91–M'93) received the M.S. and Ph.D. degrees from the Technical University of Catalonia (UPC), Barcelona, Spain, in 1988 and 1992, respectively, both in electrical engineering.

He was with the digital image sequence processing and coding group, Swiss Federal Institute of Technology—Lausanne (EPFL), Lausanne, Switzerland, from 1989 to June 1990. In June 1990, he joined the Department of Signal Theory and Communications, UPC. From June 1991 to September 1991, he was with the Signal and Image Processing Institute, University of Southern California, Los Angeles. Since 2003, he is a Full Professor at UPC, having served as Associate Dean for International Relations of the Telecommunication School (ETSETB) at UPC (1997–2000). He is currently lecturing on the area of digital signal and image processing. His current research interests include still image and sequence analysis, still image and sequence segmentation, image sequence coding, motion estimation and compensation, mathematical morphology, and biomedical applications. In these areas, he is author or coauthor of more than 80 publications that have appeared as journal papers and proceeding articles, four book chapters, and four international patents. He has served as Associate Editor of the *Journal of Electronic Imaging* in the area of Image Communications (1996–2000) and is member of the editorial board for the *Journal of Applied Signal Processing* since 2001. He was a Guest Editor for a special issue on Image Processing for 3-D Imaging for *Signal Processing: Image Communication* and a special issue on Signal Processing for 3-D Imaging and Virtual Reality for the *Journal of Applied Signal Processing*.

Dr. Marqués has served with the European Association for Signal and Image Processing (EURASIP) Administration Committee as Officer responsible for membership development (1994–1998), as an elected member responsible of the member services (1998–2000), and as Secretary and Treasurer (2000–2002). He is currently its President. He received the Spanish Best Ph.D. Thesis on Electrical Engineering Award in 1992.